Check for updates

A DFT investigation of lead-free TlSnX₃ (X = Cl, Br, or I) perovskites for potential applications in solar cells and thermoelectric devices

Redi Kristian Pingak, [iD] *[a] Soukaina Bouhmaidi,[b] Amine Harbi,[c] Larbi Setti,[b] Fidelis Nitti, [iD][d] M. Moutaabbid,[c] Albert Z. Johannes,[a] Nikodemus U. J. Hauwali[e] and Meksianis Z. Ndii[f]

In the present study, the Density Functional Theory (DFT) was employed to computationally investigate the potential application of newly developed lead-free perovskites with the formula of TlSnX₃ (X = Cl, Br, or I) as absorbers in the perovskite solar cells and as thermoelectric materials. The Quantum Espresso code was implemented to optimize the structural configuration of the perovskites and to compute a range of their properties, including their elasticity, electronic behavior, optical characteristics, and thermoelectric attributes. The findings indicated that these perovskite materials exhibit both chemical and structural stability and that TlSnBr₃ and TlSnI₃ perovskites possess high dynamic stability. The findings additionally revealed direct (R → R) band gap energy values of 0.87 eV for TlSnCl₃, 0.52 eV for TlSnBr₃, and 0.28 eV for TlSnI₃ using the GGA–PBE functional. Further analysis of their elastic properties suggested that these materials are mechanically stable and displayed overall ductile behaviour. They also demonstrated remarkable optical properties, particularly a high absorption coefficient, ranging from 10^5 cm^{-1} to 10^6 cm^{-1}. Consequently, it is reasonable to infer that these materials exhibit considerable potential for utilization in solar cells. Finally, the evaluation of their thermoelectric properties has revealed the highly promising potential of these materials to be employed in thermoelectric applications.

1 Introduction

The quest for sustainable and renewable energy sources has become a vital global mission, primarily driven by the increasing concerns on the limited supply of fossil fuels and the repercussions of climate change. Solar energy has emerged as a promising solution, with photovoltaic technologies playing a pivotal role in harnessing the power of the sun. Within this array of technologies, lead-based perovskite solar cells (PSCs) have garnered substantial interest for their remarkable potential to revolutionize the solar energy landscape due to their high-power conversion efficiency and cheap production cost.

With their unique crystalline structure and exceptional optoelectronic properties, lead-based perovskite materials have also rapidly evolved into a frontrunner in the field of photovoltaic markets, challenging the dominance of traditional silicon-based solar cells.[1–6] A recent study reported that the efficiency of lead-based PSCs reached 25.8%,[7] which is comparable to that of the conventional silicon based solar cells (26.6%).[8] Indeed, if the silicon and perovskite materials are combined in tandem solar cells, much higher efficiency can be achieved. One of the most recent studies reported that the silicon–perovskite tandem solar cells have 29.80% efficiency.[9] However, the toxicity associated with the presence of lead in these materials has risen environmental and health concerns, challenging the sustainability and safety of PSCs and thus hampering the large-scale fabrication of the PSCs.[10] Considering these challenges, the pursuit of more environmentally and sustainably lead-free perovskite materials ABX₃ has emerged as a promising avenue. This initiative has the promise not only to revolutionize the market for perovskite solar cells (PSCs) but also to streamline their large-scale production, thus effectively addressing the urgent demand for cleaner and safer energy.

Recent development in the field of lead free perovskites material has shed the light on the exceptional properties of Sn-based perovskites in comparison to other lead-free perovskites. As evidenced by a recent research by Ke and Kanatzidis (2019),

[a]Department of Physics, Faculty of Science and Engineering, The University of Nusa Cendana, Kupang, Indonesia. E-mail: rpingak@staf.undana.ac.id

[b]Laboratory of Advanced Science and Technologies, FPL, Abdelmalek Essaadi University, Tetouan, Morocco

[c]Department of Chemistry, Faculty of Sciences Ben M'Sik, Laboratory of Chemistry and Physics of Materials LCPM, University Hassan II of Casablanca, Casablanca, Morocco

[d]Department of Chemistry, Faculty of Science and Engineering, The University of Nusa Cendana, Kupang, Indonesia

[e]Department of Physics Education, The University of Nusa Cendana, Kupang, Indonesia

[f]Department of Mathematics, Faculty of Science and Engineering, The University of Nusa Cendana, Kupang, Indonesia

Sn-based perovskites have exhibited remarkable stability and have demonstrated superior performance when utilized in solar cells.[11] Notably, some recent studies have underlined the promising optoelectronic properties of Sn-based perovskites $ASnX_3$ include $CsSnX_3$ (X = I, Br, Cl),[12] $KSnCl_3$,[13] $TlSnF_3$,[14] $RbSnX_3$ (X = Cl, Br),[15,16] $InSnCl_3$,[17] and $InSnX_3$ (X = I, Br, Cl) perovskites.[18] Moreover, further investigations of Sn-based double perovskites, such as Cs_2SnI_6, have unveiled their exceptional and distinct optoelectronic characteristics when compared to other lead-free perovskites.[19] These findings highlight the growing significance of Sn-based perovskite materials in various applications, particularly within the domain of solar energy and optoelectronics.

Despite the existing studies, there has been a notable absence of studies on Sn-based halide perovskites where thallium (Tl) acts as the other cation and X represents Cl, Br or I. Indeed, the only existing studies involving such materials were conducted on $TlSnF_3$ by Pingak[14] and Zaman et al.[20] Their findings revealed that $TlSnF_3$ possesses an indirect band gap (R → M) with energy values of 0.75 eV and 0.63 eV, respectively. However, it is worth noting that the indirect nature of the energy gap in $TlSnF_3$ can be altered into a direct bandgap behavior by substituting F with Cl, Br, or I. Recent investigation by Pingak et al.[18] has demonstrated that the replacement of Cl with Br results in a change in the band gap nature of the compounds. Moreover, recent experimental research has highlighted the potential of the $TlSnI_3/C_3N_4$ nanocomposites as a viable photocatalyst for water treatment.[21] A theoretical exploration of $TlSnI_3$ in its orthorhombic structure by Singh[22] has also demonstrated that Sn is a promising activator in $TlPbI_3$, conducive to its utilization as low-band-gap scintillators. Therefore, further investigation of the properties of lead-free perovskites $TlSnCl_3$, $TlSnBr_3$, and $TlSnI_3$ is of considerable significance.

The objective of the present study is to conduct a comprehensive investigation into the optoelectronic, elastic, and thermoelectric properties of $TlSnX_3$ (where X can be Cl, Br, or I) perovskite materials. This investigation utilizes the Density Functional Theory (DFT) method, which is known as a highly effective and accurate computational approach for predicting the properties of novel materials. By using DFT method in this research, we aim to obtain the precise material properties prior to the experimental synthesis. This will provide comprehensive information which can streamline the potential application of the studied perovskite materials in various devices and technologies.

2 Computational details

The computation of the properties of the $TlSnX_3$ (X = Cl, Br, I) perovskites was conducted using the Quantum Espresso (QE) code[23] based on the DFT approximation,[24] with GGA-PBE functional.[25] Although the PBE functional generally underestimates materials' band gap energy, Råsander and Moram[26] observed that it exhibits relatively comparable accuracy to other functionals, including hybrid functionals in generating materials' lattice constants. Surprisingly, certain elastic properties of the

materials derived from the PBE functional are even more accurate than those obtained from other functionals. The procedures involved in the calculation of the properties are as follows. First, the total energy of the compounds as a function of lattice parameters was calculated. Then, the cell relaxation was conducted to optimize the structure of the $TlSnX_3$ (X = Cl, Br, I) perovskites. This was done based on the Birch–Murnaghan equation of states,[27,28] using eqn (1).

$$E(V) = E_0 + \frac{B}{B'(B'-1)}\left[V\left(\frac{V_0}{V}\right)^{B'} - V_0\right] + \frac{B}{B'}(V - V_0) \quad (1)$$

In this self-consistent field calculation, we applied k-points of size 6 × 6 × 6. The optimized lattice parameters of the compounds were then used to perform non-self-consistent calculation, with k-points of size 12 × 12 × 12, to calculate their electronic properties. Energy cut-offs for the wave function and the charge density were 50 Ry and 500 Ry, respectively, while the total energy convergence threshold was set to be 10^{-8} Ry.

To evaluate the chemical stability of the perovskites, their formation energies were also computed using eqn (2), where the total energy of $TlSnX_3$ (X = Cl, Br, I) unit cell is represented by E_{tot} ($TlSnX_3$) while the energy of Tl, Sn, and X (X = Cl, Br, I) atoms is represented by $E(Tl)$, $E(Sn)$ and $E(X)$ for the respective atoms.

$$\Delta E_f = \frac{E_{tot}(TlSnX_3) - E(Tl) - E(Sn) - 3E(X)}{5} \quad (2)$$

Meanwhile, the optical and elastic properties of the perovskites were computed using the thermo pw program and the thermoelectric properties were calculated using the BoltzTrap code,[29] within which the fixed relaxation time approximation is applied. The 3D representation of the Young's modulus, shear modulus, and bulk modulus of the studied compounds are also plotted using the ELATE code. The imaginary part of dielectric function $\varepsilon_2(\omega)$ was calculated using eqn (3) while and the real part $\varepsilon_1(\omega)$ was calculated using eqn (4),[30–34] where the electronic charge is represented by e and the unit cell volume is represented by Ω. Meanwhile, ψ_k^V and E_K^V are the wave functions and the electrons' energy at a particular k in the valence bands, respectively, whereas ψ_k^C and E_K^C are those in the conduction band, respectively. Finally, U is the unit vector along polarization direction of the electric field of the incident light.

$$\varepsilon_2(\omega) = \frac{2e^2\pi}{\Omega\varepsilon_0}\sum_{k,V,C}\left|\left\langle\psi_k^C|\vec{U}\cdot\vec{r}|\psi_k^V\right\rangle\right|^2\delta\left(E_K^C - E_K^V - E\right) \quad (3)$$

$$\varepsilon_1(\omega) = 1 + \frac{2}{\pi}P\int_0^\infty \frac{\omega'\varepsilon_2(\omega)'}{\omega'^2 - \omega^2}d\omega' \quad (4)$$

Other optical properties including the refractive index $\eta(\omega)$, the extinction coefficient $k(\omega)$, the reflectivity $R(\omega)$, the absorption coefficient $\alpha(\omega)$, and the loss function $L(\omega)$ of the perovskites were calculated using eqn (5)–(9), respectively.[34]

$$\eta(\omega) = \frac{1}{\sqrt{(2)}}\left[\left(\varepsilon_1(\omega)^2 + \varepsilon_2(\omega)^2\right)^{1/2} + \varepsilon_1(\omega)\right]^{1/2} \quad (5)$$

$$k(\omega) = 1 + \frac{1}{\sqrt{(2)}}\left[\left(\varepsilon_1(\omega)^2 + \varepsilon_2(\omega)^2\right)^{1/2} - \varepsilon_1(\omega)\right]^{1/2} \quad (6)$$

$$R(\omega) = \frac{(\eta - 1)^2 + k^2}{(\eta + 1)^2 + k^2} \quad (7)$$

$$\alpha(\omega) = \frac{2\omega}{c}k(\omega) \quad (8)$$

$$L(\omega) = \frac{\varepsilon^2}{\varepsilon_1{}^2 + \varepsilon_2{}^2} \quad (9)$$

3 Results and discussion

3.1 Structural properties

The perovskite crystals TlSnX$_3$ (X = Cl, Br, or I) exhibit a cubic structure, and their crystal structure falls within the space group $Pm\bar{3}m$ (number 221). The unit cell structure of TlSnCl$_3$

Fig. 1 Unit cell structure of the cubic TlSnCl$_3$ perovskite.

perovskite is visualized in Fig. 1, where the Tl cations are situated at the Wyckoff coordinates of (0, 0, 0) while the Sn atom is located at (0.5, 0.5, 0.5); meanwhile, the remaining three Cl anions are positioned at (0.5, 0.5, 0), (0.5, 0, 0.5), and (0, 0.5, 0.5). The unit cell of TlSnBr$_3$ and TlSnI$_3$ perovskites is identical to that of TlSnCl$_3$, with Cl replaced by Br and I, respectively.

Total energy as a function of the lattice parameter of TlSnX$_3$ (X = Cl, Br, I) perovskites is shown in Fig. 2. The graph clearly indicates a noticeable shift in the equilibrium lattice parameters of these compounds when the X anions are altered. This outcome was anticipated because of the clear difference in the ionic radii of the respective anions.

Table 1 depicts the calculated optimized lattice constants for the studied perovskites. As observed from Table 1, there is a systematic increase in the lattice parameters when Cl is substituted with Br, and then with I. This phenomenon arises from the expansion of the compounds' unit cells, driven by the increased ionic radii resulting from the substitution, which is necessary for achieving stability and minimizing the total energy. This observation is consistent with the findings of a recent study on isoelectronic compounds like InSnX$_3$ (X = Cl, Br, I) perovskites.[18] This also corresponds with similar trends reported for a wide range of ABX$_3$ perovskites[35–41] and double perovskites.[42–49]

Another important parameter is the formation energy of these compounds, which is closely related to their chemical stability. The formation energy values for the compounds are presented in Table 1. Since the TlSnX$_3$ (X = Cl, Br, I) perovskites have negative formation energy, it can be predicted that these perovskite materials are chemically stable and thus they can be experimentally synthesized under standard ambient condition.

In addition, the analysis of phonon dispersion profiles can be used as valuable tools to study the dynamic stability of materials. Therefore, the phonon dispersion of TlSnX$_3$ (X = Cl, Br, I) perovskites was calculated in the present work and the results were displayed in Fig. 3. As evident from Fig. 3, the lattice vibrational frequency for all phonon modes in TlSnBr$_3$ and TlSnI$_3$ are positive, indicating their dynamic stability. Moreover, the presence of three acoustic branches with zero frequency at the $k = 0$ point in the reciprocal space further confirms the materials' dynamic stability. This behaviour aligns with the results reported for other perovskites.[50,51] In contrast, TlSnCl$_3$ perovskite possesses a negative frequency at the M-point, suggesting that the material is not as stable as the TlSnBr$_3$ and TlSnI$_3$ perovskites.
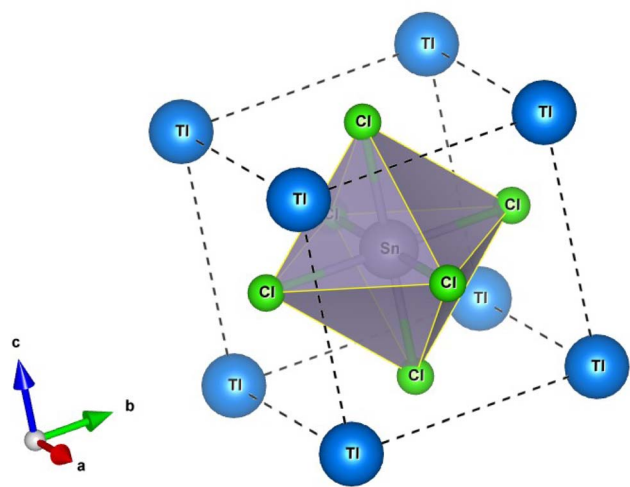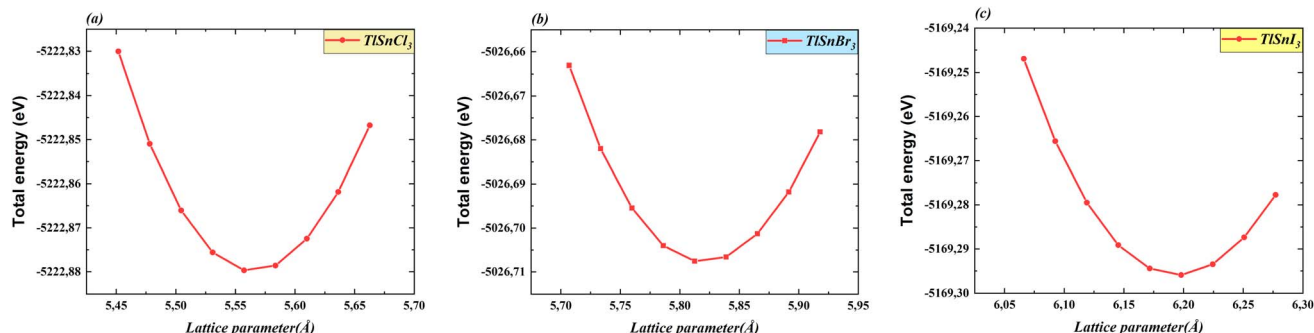

Fig. 2 Total energy as a function of the lattice constants of the cubic TlSnCl$_3$ (a), TlSnBr$_3$ (b), and TlSnI$_3$ (c) perovskites.

Table 1 The optimized lattice constants a, the formation energy ΔE_f, and energy band gaps E_g of the cubic $TlSnX_3$ (X = Cl, Br, I) perovskites from the GGA-PBE approximation

Perovskites	a (Å)	ΔE_f (eV)	E_g (eV):GGA
$TlSnCl_3$	5.58	−3.11	0.87 (R → R)
$TlSnBr_3$	5.83	−2.79	0.52 (R → R)
$TlSnI_3$	6.21	−2.44	0.28 (R → R)

The appearance of imaginary modes in the phonon dispersion might stem from three factors: (i) potential numerical issues during the calculation, (ii) incomplete consideration of certain physical parameters when computing dynamical matrices or force constants, and (iii) inherent dynamic instabilities within the crystal structure.[52] Given that the numerical methods and physical parameters used for $TlSnCl_3$, $TlSnBr_3$, and $TlSnI_3$ are identical, factors (i) and (ii) are eliminated, suggesting that the appearance of the imaginary mode in the phonon dispersion of $TlSnCl_3$ corresponds to intrinsic instabilities within the perovskite's crystal. This situation could represent either a local maximum or a saddle point on the Potential Energy Surface (PES) and might be accessed as an average over nearby minima at elevated temperatures.[52]

3.2 Electronic properties

This section provides the calculated energy band diagrams and the electronic density of $TlSnX_3$ (X = Cl, Br, I) perovskites. The

band diagrams for these materials are plotted in Fig. 4, where it is obvious that $TlSnCl_3$, $TlSnBr_3$, and $TlSnI_3$ perovskites exhibit direct band gaps (R → R). Furthermore, the band gap reduces as Cl is replaced with Br and I. The specific numerical values of these forbidden energy gaps are summarized in Table 1.

As evident from Fig. 4, the overall features of the band diagram of the three perovskites are notably similar, which aligns with the expected characteristics, since these materials are isoelectronic with one another. Nevertheless, a significant change is observed in the size of the forbidden gap between the valence band and conduction band of these materials. This decrease in the band gap of these compounds can be attributed to the distinct orbitals associated with the X anions. This phenomenon was also true for a wide range of halide perovskites and double perovskites. It results from an increase in the lattice parameter and bond length of the compounds, making the valence electrons less tightly bound to their parent atoms.

Moreover, the electronic band gap values of the cubic $TlSnCl_3$, $TlSnBr_3$, and $TlSnI_3$ perovskites are 0.87 eV, 0.52 eV, and 0.28 eV, respectively (Table 1). More importantly, the band gap of the materials is direct in nature. If one compares this with the band gap nature of $TlSnF_3$,[14,20] which is indirect, it is apparent that changing the F anion by Cl, Br, or I anions results in the change in the bandgap nature of the perovskites. This is vitally important because direct bandgap materials are better for optoelectronic applications than those with indirect nature electronic bandgap as in general, materials which have direct bandgap experience faster carrier recombination and have
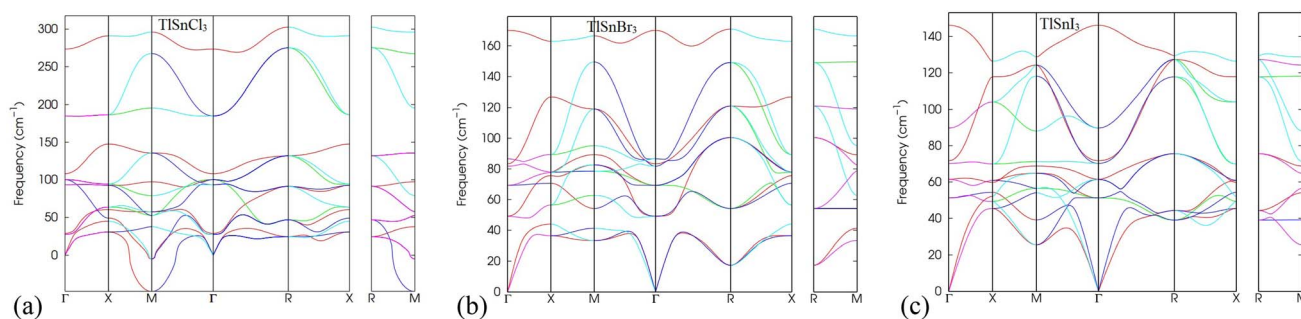

Fig. 3 Phonon dispersion curves of the cubic $TlSnCl_3$ (a), $TlSnBr_3$ (b), and $TlSnI_3$ (c) perovskites.
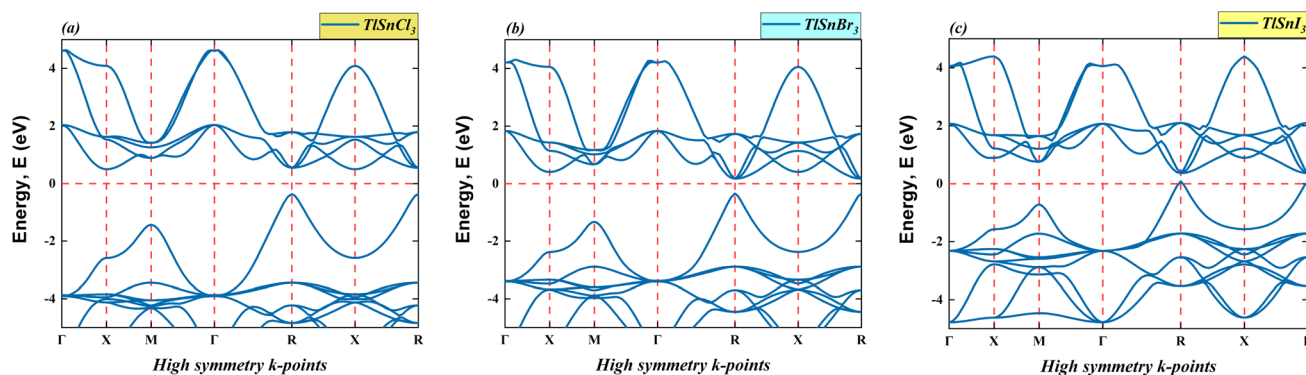

Fig. 4 Energy band diagram of the cubic $TlSnCl_3$ (a), $TlSnBr_3$ (b), and $TlSnI_3$ (c) perovskites.

better radiative efficiency than those that possess indirect bandgap.[53] In their study, Wang *et al.*[53] managed to induce indirect-to-direct bandgap transition in the methylammonium lead iodide *via* external hydrostatic pressure. Various methods that successfully change indirect nature of bandgap into direct one were also reported in a number of studies, including mechanical strains,[54] order-to-disorder transformation,[55] mixing of cations,[56] and thermal approach.[57] The studies observed that the change in the bandgap nature of materials leads to change in their optical properties.

To evaluate the chemical bonds within the compounds, we have plotted their (110) electron density, shown in Fig. 5. The electron density provides information about the charge distribution within the unit cell of the materials, from which the nature of the chemical bonds present in the materials can be determined. These figures clearly indicate that the Tl–Cl, Tl–Br, and Tl–I bonds are mainly ionic in nature. This is evident from the nearly spherical electronic distribution around these atoms. Conversely, the Sn–Cl, Sn–Br, and Sn–I bonds are predicted to be mainly covalent, as evident by an obvious distortion in the electron distribution between the

atoms. Consequently, it can be inferred that the replacement of the halogen does not significantly alter the bonding characteristics of these compounds, as Tl–X and Sn–X bonds remain predominantly ionic and covalent, respectively, irrespective of the specific X anion. This observation aligns with the characteristics of other ABX_3 perovskites including oxide (X = O),[58–60] halide (X = Cl, Br, I) perovskites[61] and anti-perovskites.[62] Across these structures, the A–X bonds generally exhibit an ionic nature,[63] consistent with the findings in our study where Tl–X is identified as predominantly ionic. Simultaneously, the B–X bonds predominantly demonstrate a covalent nature, which corresponds to our observations where the Sn–X bond exhibits a mainly covalent character. Notably, these B–X bonds significantly govern the optoelectronic properties of the perovskites and play a pivotal role in their exceptional optical absorption, a critical aspect for their applications in solar cells.[63] These bonding characteristics observed in $TlSnX_3$ closely resemble those observed in $InSnX_3$ (X = Cl, Br, I) perovskites,[14] where it was reported that the covalent character percentages of Sn–Cl, Sn–Br, and Sn–I are predicted to be approximately 77.11%, 81.06%, and 87.37%, respectively.
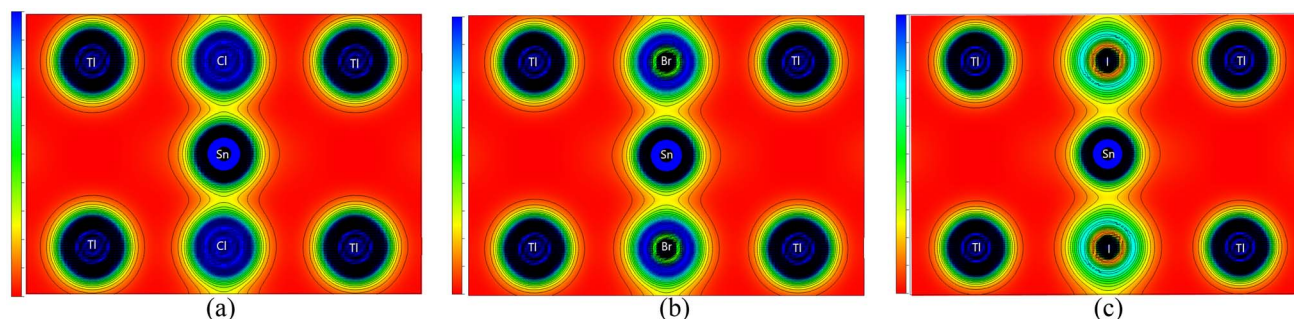

Fig. 5 (110) electron density of the cubic $TlSnCl_3$ (a), $TlSnBr_3$ (b), and $TlSnI_3$ (c) perovskites.

Table 2 Elastic properties of the cubic $TlSnX_3$ (X = Cl, Br, I) perovskites from the GGA functional

Parameters	$TlSnCl_3$	$TlSnBr_3$	$TlSnI_3$
Elastic const. C_{11} (GPa)	51.52	45.44	37.99
Elastic const. C_{12} (GPa)	8.81	6.78	4.39
Elastic const. C_{44} (GPa)	3.38	2.89	2.66
Bulk modulus B (GPa)	22.99	19.70	15.59
Shear modulus G (GPa)	7.81	6.94	6.17
Pugh ratio B/G	2.94	2.84	2.53
Anisotropy factor A	0.16	0.15	0.158
Young's modulus E (GPa)	20.82	18.39	16.14
Poisson ratio ν	0.33	0.32	0.31
Kleinman parameter ξ	0.32	0.30	0.27
Cauchy pressure ($C_{12} - C_{44}$)	5.43	3.89	1.73
Debye temperature θ_D (K)	128.356	107.025	93.462
Melting temperature T_m (K)	857.53 ± 300	822.25 ± 300	777.56 ± 300
Average sound velocity V_m (m s^{-1})	1406.33	1226.18	1140.30
Longitudinal sound velocity V_l (m s^{-1})	2365.767	2045.524	1788.201
Transverse sound velocity V_t (m s^{-1})	1379.006	1213.807	1124.479
Lamé const. λ	4.12	3.50	2.96
Lamé const. μ	7.83	6.96	6.16
Total mass (a.m.u)	429.4433	562.7933	703.8053
Density (g cm^{-3})	4.1083	4.7088	4.8761

3.3 Elastic properties

Table 2 presents the calculated elastic properties of the $TlSnCl_3$, $TlSnBr_3$, and $TlSnI_3$ compounds. Among the most significant elastic properties of the materials are their elastic constants, as they can be used to assess the mechanical stability of the materials using the well-known Born–Huang mechanical stability criteria.[64] The mechanical stability of materials is confirmed when their bulk modulus B and elastic constants satisfy specific conditions, which include $C_{11} > 0$, $C_{44} > 0$, $(C_{11} - C_{12}) > 0$, $(C_{11} + 2C_{12}) > 0$, and $C_{12} < B < C_{11}$. Based on the calculated data presented in Table 2, it is apparent that the elastic constants and the bulk modulus of all the three studied perovskites satisfy these criteria, confirming their mechanical stability.

The bulk modulus B, provides insights into the perovskites' resistance to applied pressure. From Table 2, it can be seen that $TlSnCl_3$ perovskite has the highest bulk modulus B (22.99 GPa), followed by $TlSnBr_3$ (19.70 GPa) and finally by $TlSnI_3$ (15.59 GPa). This implies that $TlSnCl_3$ is predicted to be more resistant to external pressure compared to its counterparts $TlSnBr_3$ and $TlSnI_3$ perovskites. Interestingly, the decrease in the bulk modulus of these compounds as Cl is replaced by Br and I is also accompanied by a reduction in the materials' energy gap. This linear relationship between bulk modulus and energy gap has been predicted for a large number of materials.[65] However, it is worth noting that this relationship might not be applicable universally, as Li *et al.*[66] found that for alloys, this trend is not always true. They argued that various factors, including size and chemical effects, play a major role in the variation of the band structure in alloys.[67]

The shear modulus G is another important parameter which describes the shear resistance of materials. Similar to the bulk modulus, the $TlSnCl_3$ is expected to have larger shear resistance than $TlSnBr_3$ and $TlSnI_3$. Similarly, concerning the stiffness of the perovskites, represented by their Young's modulus E, $TlSnCl_3$ perovskite is the stiffest material compared to its counterparts.

From the Poisson and the Pugh's ratio, one can predict the ductility of materials. A material is considered ductile if its Poisson ratio is greater than 0.26; and brittle if it is lower than 0.26.[68] Moreover, a material is ductile if its Pugh's ratio is larger than 1.75 and is brittle if its Pugh's ratio is lower than 1.75.[69] As indicated by Table 2, the studied perovskites are all predicted to possess ductile behaviour since their Poisson ratio and Pugh's ratio are larger than 0.26 and 1.75, respectively. This prediction is also corroborated by the positive values of the Cauchy pressure for these perovskites.

To investigate internal strain within the studied perovskites, their Kleinman parameter ξ was computed, with computed Kleinman parameter of 0.32, 0.30, and 0.27 for $TlSnCl_3$, $TlSnBr_3$, and $TlSnI_3$, respectively. These values suggest that within the perovskites structure, the bond bending is more dominant than the bond stretching. In the context of Kleinman parameters, $\xi = 0$ corresponds to minimizing bond bending and $\xi = 1$ corresponds to minimizing bond stretching.[70]

It is observed that the Debye temperature and the melting temperature of the perovskite materials decrease as Cl is replaced by Br and I. This trend is also reflected in their longitudinal, transverse and average sound velocity. On the other hand, their total mass and density increase following the anion replacement.

Finally, the two Lamé's constants can be used to further investigate the perovskites' elastic behaviour. The first Lamé's constant λ and the second constant μ measure their compressibility and shear stiffness.[71,72] It is expected that these two constants should be directly proportional to the values of the Young modulus, which is confirmed in the present study (Table 2). Furthermore, the change in the second Lamé's constant should mirror the variation in the shear modulus, as both represent the shear behaviour of the compounds. As expected, this relationship is also confirmed in the current study, and has been reported for various isoelectronic materials.[73–76]

Furthermore, the 3D elastic properties such as the linear compressibility, shear modulus and Young's modulus, of the compounds were also calculated and the results are visualized using the ELATE program (Fig. 6). It is clear that $TlSnI_3$ has the largest compressibility, followed by $TlSnBr_3$ and $TlSnCl_3$. This is in good agreement with the values of the bulk modulus as presented in Table 2 since the compressibility is inversely proportional to the bulk modulus. The 3D profiles of the elastic properties can also be used to predict the anisotropy of the mechanical properties of the perovskites. The high degree of deviation from the 3D shapes of their shear modulus and Young's modulus strongly indicates elastic anisotropy and therefore, the materials are predicted to possess interesting elastic anisotropy. The anisotropy can be further analyzed from the minimum and maximum values of the corresponding properties of the materials, which are summarized in Table 3 along with those of the Poisson ratio ν.

The considerable difference between the minimum and the maximum values of the shear modulus G and the Young's modulus E confirms the high degree of the anisotropy of the two mechanical properties within the studied perovskites. The computed minimum values of the shear modulus of $TlSnCl_3$, $TlSnBr_3$, and $TlSnI_3$ perovskites are 3.38 GPa, 2.89 GPa, and 2.66 GPa, respectively, far lower than its maximum values: 21.36 GPa, 19.39 GPa, and 15.57 GPa for the respective materials. Similarly, the computed minimum (maximum) values of their Young's modulus are 9.67 GPa (48.95 GPa), 8.27 GPa (43.79 GPa), and 7.58 GPa (36.50 GPa) for $TlSnCl_3$, $TlSnBr_3$, and $TlSnI_3$ compounds, respectively. Interestingly, the minimum values of their shear modulus and the maximum values of their Young's modulus are found along the same [001] direction. This implies that the three studied perovskites are predicted to be more resistant to any external pressure along the [001] direction than other crystal orientations within the materials, and at the same time have lower shear resistance in this direction compared to the other directions within the materials.

It is also interesting to note that although our calculated Poisson's ratio in Table 2 indicates that the materials are all ductile in nature, the Poisson's ratio extracted from the 3D profiles of the elastic properties of $TlSnCl_3$, $TlSnBr_3$, and $TlSnI_3$ compounds range from 0.04 to 0.79, 0.03 to 0.79, and 0.03 to 0.78, respectively. This strongly indicates that although it is
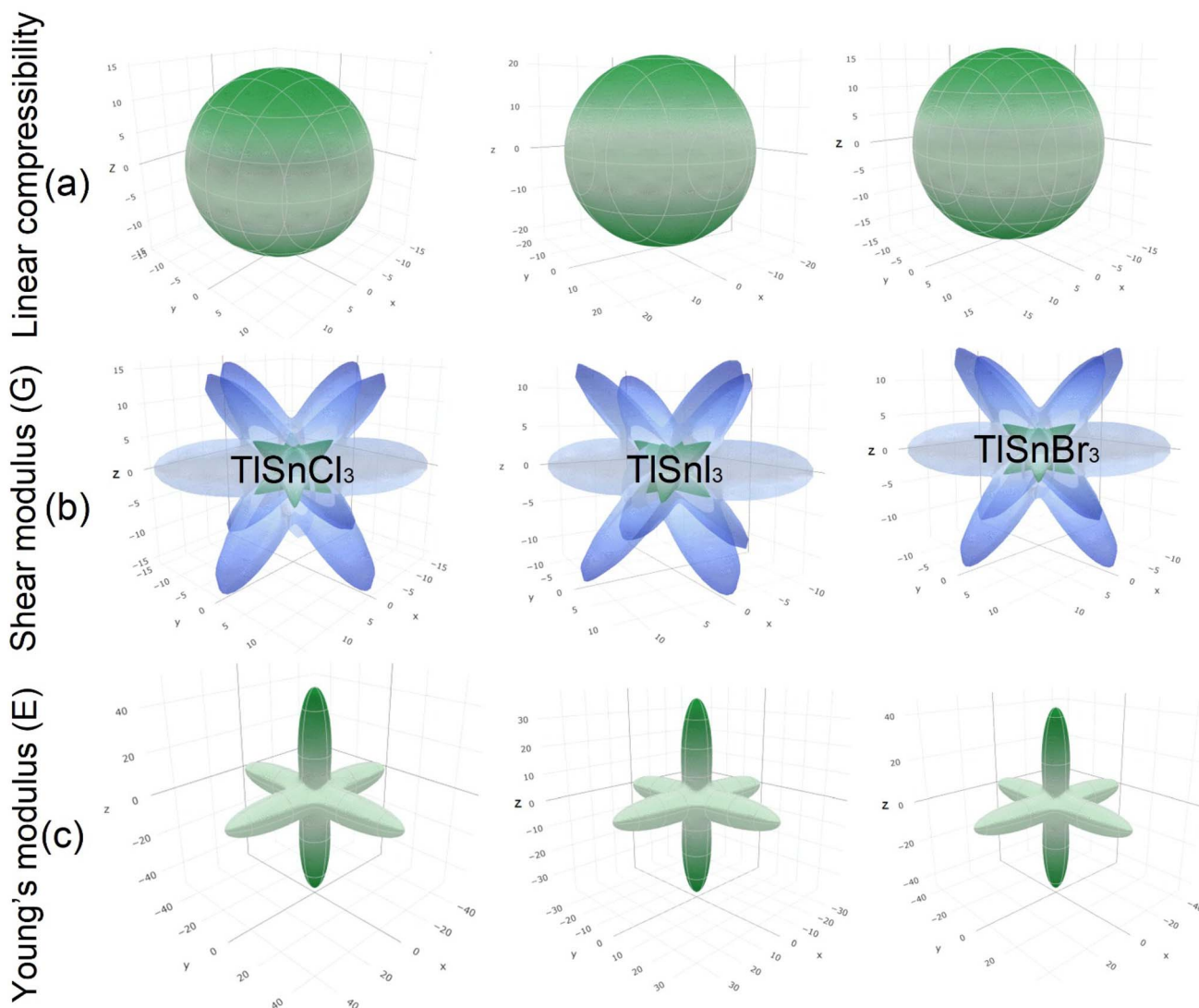
Fig. 6 3D elastic properties of the cubic TlSnCl₃, TlSnBr₃, and TlSnI₃ perovskites: linear compressibility (a), shear modulus (b), Young's modulus (c).

Table 3 The minimum and maximum values of E (GPa), G (GPa), and ν of the cubic TlSnX₃ (X = Cl, Br, I) perovskites

Perovskites	G_{min}	G_{max}	E_{min}	E_{max}	ν_{min}	ν_{max}
TlSnCl₃	3.38	21.36	9.67	48.95	0.04	0.79
TlSnBr₃	2.89	19.39	8.27	43.79	0.03	0.79
TlSnI₃	2.66	15.57	7.58	36.50	0.03	0.78

predicted that the materials exhibit overall ductility, they may show brittleness in some directions within the crystal of the materials. Furthermore, the results also indicate that the materials exhibit similar ductile behaviour even though TlSnCl₃ is projected to be slightly more ductile.

The 3D contours of the Young's moduli of materials are also strongly correlated to the types of octahedral connection within them.[77–79] The shape of the 3D Young's moduli profiles of the compounds represents Sn–X (X = Cl, Br, I) bonds along the ⟨001⟩ family planes, which is also closely related to the charge distribution between Sn and X atoms as shown in Fig. 5. Similar finding was also reported for Pb–I bonds in γ-CsPbI₃.[79]

3.4 Optical properties

The optical properties of the TlSnX₃ (X = Cl, Br, I) perovskites were calculated within photon energy interval [0, 20] eV. The computed real part of the dielectric function $\varepsilon_1(\omega)$, the imaginary part $\varepsilon_2(\omega)$, and the refractive index $\eta(\omega)$ of the perovskite compounds are shown in Fig. 7.

It is noticeable from Fig. 7 is that the overall feature of the refractive index of the compounds (Fig. 7c) resembles that of the dielectric function $\varepsilon_1(\omega)$ (Fig. 7a), as expected. It is also obvious from Fig. 7a that the TlSnI₃ perovskite has the highest static dielectric function $\varepsilon_1(0)$ of 7.75, which is followed by TlSnBr₃ and TlSnCl₃ perovskites with static dielectric function of 6.20 and 5.13, respectively. This indicates that, based on their $\varepsilon_1(0)$
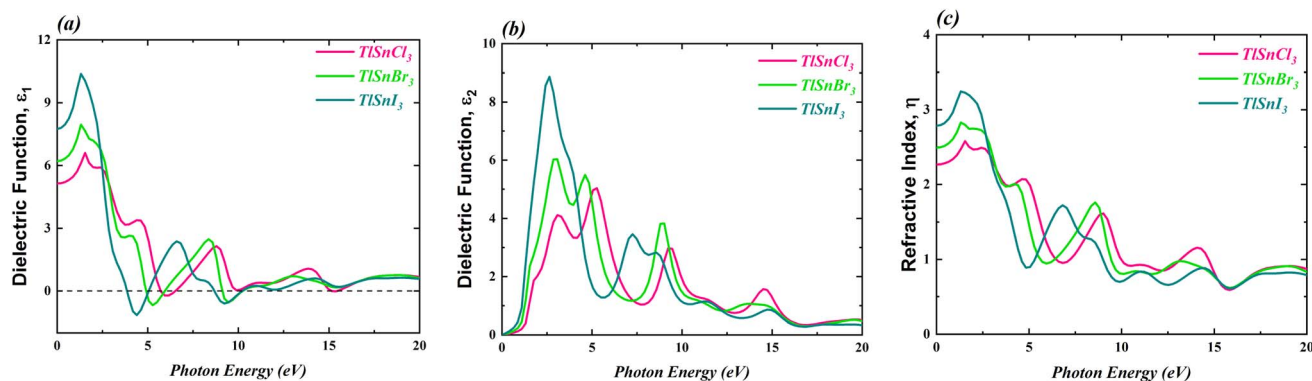
Fig. 7 $\varepsilon_1(\omega)$ (a), $\varepsilon_2(\omega)$ (b), and $\eta(\omega)$ (c) of the cubic TlSnCl$_3$, TlSnBr$_3$, and TlSnI$_3$ perovskites.

values, TlSnI$_3$ is expected to exhibit better optoelectronic performance compared to TlSnBr$_3$ and TlSnCl$_3$. This is due to the fact that materials with larger $\varepsilon_1(0)$ values tend to have lower charge recombination,[80,81] which is favourable for optoelectronic applications. In addition, there is an inverse relationship between $\varepsilon_1(0)$ and the energy band gaps of the TlSnCl$_3$, TlSnBr$_3$, and TlSnI$_3$ compounds, which aligns with the Penn model.[82] Similarly, the static refractive index values $\eta(0)$ also increase when Cl is substituted by Br and I. The $\eta(0)$ values of TlSnCl$_3$, TlSnBr$_3$, and TlSnI$_3$ perovskites are 2.27, 2.49, and 2.78, respectively.

The imaginary part of the $\varepsilon_2(\omega)$, as shown in Fig. 7b, provides insights into the perovskites' absorption behaviour. The strongest absorption by these studied perovskites can be predicted

from the main peaks of their calculated absorption spectra, represented by the $\varepsilon_2(\omega)$ graph. In line discussion of the compounds' band structure in the previous section, where it was found that the band gap of the materials decrease as Cl is replaced by Br and I, Fig. 7b also indicates a shift in the energy threshold of $\varepsilon_2(\omega)$ to lower photon energy due to the anion replacement. Beyond this energy threshold, the absorption of TlSnCl$_3$, TlSnBr$_3$, and TlSnI$_3$ perovskites is predicted to increase, reaching their main absorption peaks at approximately 5.03, 6.03, and 8.87, at approximately 5.28 eV, 3.08 eV, and 2.64 eV, for the respective perovskite materials.

To further investigate the optical properties of the compounds, the dielectric constants were used to calculate the reflectivity $R(\omega)$, the absorption coefficient $\alpha(\omega)$, the loss
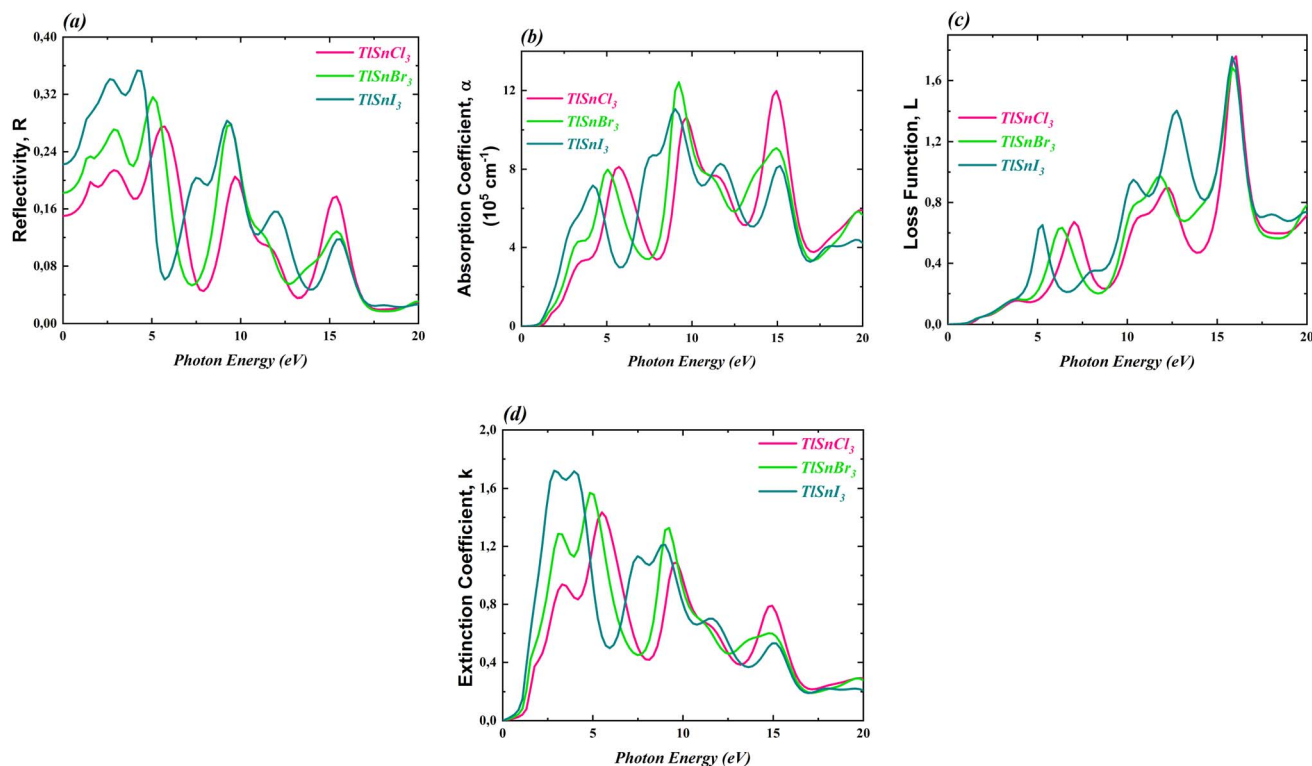

Fig. 8 $R(\omega)$ (a), $\alpha(\omega)$ (b), $L(\omega)$ (c) and $k(\omega)$ (d) of the cubic TlSnCl$_3$, TlSnBr$_3$, and TlSnI$_3$ perovskites.

function $L(\omega)$, and the extinction coefficient $k(\omega)$. These properties are important to evaluate the potential application of the materials in optoelectronic devices. The computed corresponding properties are presented in Fig. 8.

Fig. 8a reveals that the reflectivity of the compounds is relatively low. The maximum reflectivity of $TlSnCl_3$, $TlSnBr_3$, and $TlSnI_3$ is 27.52% at 5.72 eV, 31.62% at 5.06 eV, and 35.31% at 4.18 eV, respectively. Additionally, the materials exhibit strong absorption, in the order of 10^5 cm^{-1} to 10^6 cm^{-1} (Fig. 8b). The threshold energy for absorption aligns with the electronic band gap energy of the compounds as well as the threshold energy for the imaginary part of the dielectric function. This further confirms that $TlSnI_3$ has the lowest optical band gap energy and thus can absorb light of lower energy. The high absorption of the $TlSnI_3$ perovskite was previously predicted by Singh[22] for the orthorhombic phase. It is also important to note a significant dissimilarity between the absorption threshold reported by Singh (around 2 eV) and our finding (approximately 0.4 eV). This divergence can be attributed to the different structures considered in the two studies. Recently, Ghaithan et al.[83] disclosed that using several functionals, the orthorhombic structure of $CsPbBr_3$ exhibits a marginally larger energy gap compared to its cubic structure. Similar trends were also observed for other perovskites including $BaZrS_3$,[84] $CH_3NH_3PbI_3$,[85] and $PbZrO_3$.[86] Moreover, the discrepancy between the absorption threshold obtained by Singh and our findings can be attributed to the use of different functionals. While Singh[22] employed the TB-mBJ functional, we utilized the GGA-PBE approach, renowned for its tendency to underestimate the band gap, thereby leading to an expected lower absorption threshold in our study. This discrepancy can be further investigated using experimental data such as UV-Vis spectra, from which the optical band gap can be determined using the Tauc plot method.[87] The combination of the low reflectivity and the high absorption makes these materials potential candidates for a wide range of applications, including use as absorbers in solar cells.

Regarding the loss function $L(\omega)$, which accounts for an inelastic scattering process, Fig. 8c indicated that for low photon energy (between 0 and 3 eV), the inelastic scattering is negligibly small and therefore it does not significantly impact the absorption behaviour of the materials within this photon energy range. The loss function for the $TlSnX_3$ (X = Cl, Br, I) then increases with a similar trend above this energy except that there is a shift of the function of $TlSnI_3$ and $TlSnBr_3$ towards a lower energy between energy range about 3 eV and 10 eV. A similar shift is also observed in the extinction coefficient $k(\omega)$ of the studied perovskites, as presented in Fig. 8d. The main peaks of $k(\omega)$ of $TlSnCl_3$, $TlSnBr_3$, and $TlSnI_3$ are 1.43 at 5.50 eV, 1.57 at 4.84 eV, and 1.72 at 2.86 eV, respectively.

3.5 Thermoelectric properties

The thermoelectric properties of the cubic $TlSnX_3$ (X = Cl, Br, I) perovskites were also calculated and the computed properties are shown in Fig. 9. The properties include the electrical conductivity, the Seebeck coefficient, the thermal conductivity, and the figure of merit. All these properties were investigated as functions of the temperature.
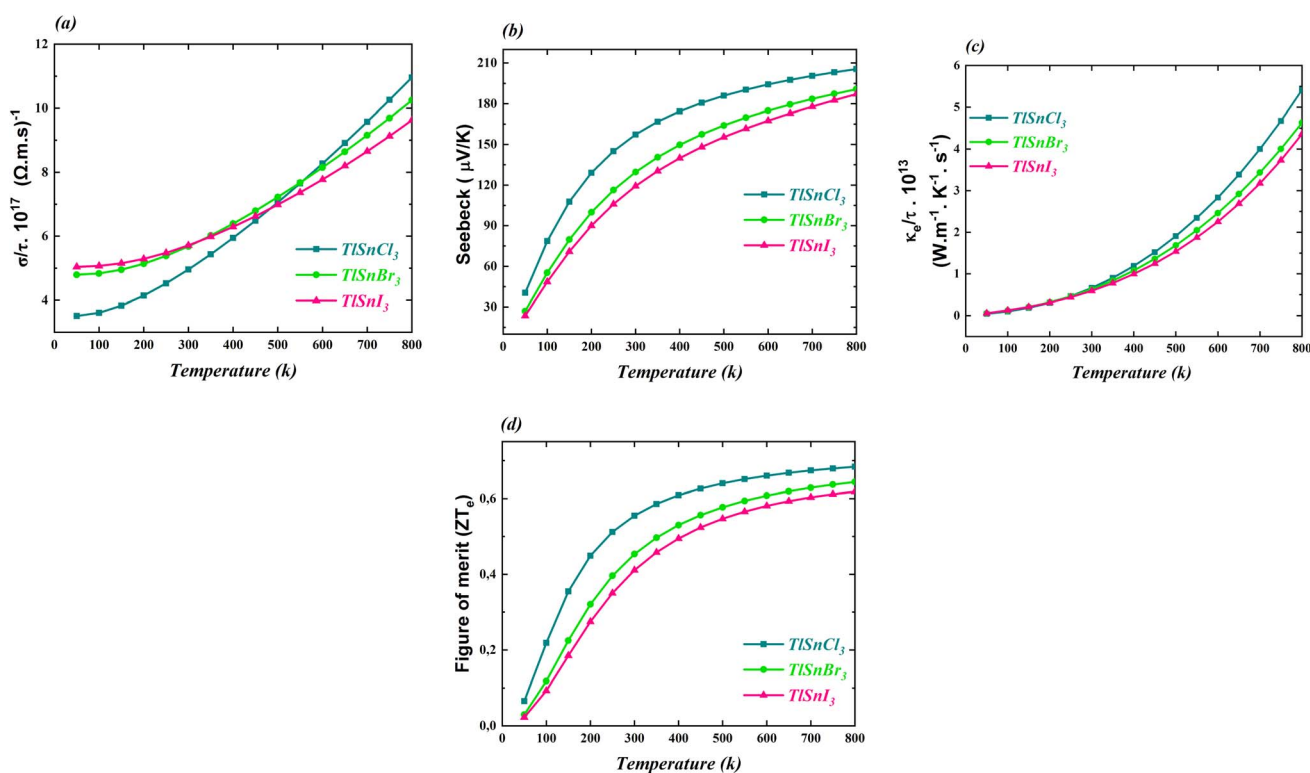

Fig. 9 (a) The electrical conductivity, (b) Seebeck coefficient, (c) thermal conductivity, and (d) figure of merit of the cubic $TlSnCl_3$, $TlSnBr_3$, and $TlSnI_3$ perovskites.

It is obvious from Fig. 9a that the electrical conductivity per relaxation time σ/γ of the three studied perovskites increases as the temperature increases. It is also notable that below 500 K, σ/γ values of TlSnI$_3$ and TlSnBr3 are considerably higher than those of TlSnCl$_3$ while for larger temperature, the reverse trend is observed. Similarly, there is an increase in the electronic contribution to the thermal conductivity of the perovskites, as depicted in Fig. 9c. The three compounds exhibit approximately the same thermal conductivity up to the room temperature (300 K). However, for temperatures above 300 K, their thermal conductivity rises considerably, with TlSnCl$_3$ having higher thermal conductivity than TlSnBr$_3$ and TlSnI$_3$ perovskites. The increase in the electrical conductivity and thermal conductivity of the studied perovskites as a function of the temperature was also observed for other isoelectronic compounds of the form InSnX$_3$ (X = Cl, Br, or I).[18]

Fig. 9b and d illustrate how the Seebeck coefficients S and the figure of merit ZT_e, respectively, change with temperature. The Seebeck coefficient measures the potential difference between two different conductors or semiconductors when a temperature gradient exists between the two junctions, while the $ZT_e = S^2 T\sigma/\kappa$ serves as a transport parameter used to assess the performance of thermoelectric materials.[88] Here, S, T, σ, and κ stand for the Seebeck coefficient, temperature, electrical and thermal conductivity, respectively. As expected, the general feature of the two parameters is very similar. As observed in both figures, these parameters increase with increasing temperature. Between 50 K and 300 K, there is a significant increase in the parameters, followed by a more gradual increase for higher temperatures. TlSnCl$_3$ has the largest Seebeck coefficient and the figure of merit for the entire temperature range, followed consecutively by TlSnBr$_3$ and TlSnI$_3$ perovskites. Since ZT_e describes the thermoelectric performance of materials, with higher ZT_e indicating better thermoelectric properties,[19] these figures clearly show that TlSnCl$_3$ is expected to have better thermoelectric performance compared to TlSnBr$_3$ and TlSnI$_3$ perovskites. The highest values of the figure of merit for the respective compounds are 0.68, 0.64, and 0.62 at 800 K. These relatively high ZT_e values suggest that these materials are promising candidates as thermoelectric materials. Virtually, all materials have positive Seebeck coefficients, indicating that they are highly likely p-type semiconductors.

4 Conclusions

In this study, a comprehensive computational investigation on the structural, elastic, optoelectronic, and the thermoelectric properties of novel lead-free perovskites with the chemical composition TlSnX$_3$ (X = Cl, Br, I) was conducted using the DFT based on the GGA-PBE functional. The results showed that the studied perovskites are structurally and mechanically stable and that TlSnBr$_3$ and TlSnI$_3$ perovskites are also dynamically stable. They were also found to be ductile in nature and possess direct semiconducting behaviour, with GGA-PBE electronic band gaps of 0.87 eV, 0.52 eV, and 0.28 eV for TlSnCl$_3$, TlSnBr$_3$, and TlSnI$_3$, respectively. Moreover, the perovskites have outstanding optical properties making them promising for applications in optoelectronics including perovskite solar cells. Analysis of their thermoelectric properties also suggested that the perovskites can be used as thermoelectric materials.

Conflicts of interest

There are no conflicts to declare.

Acknowledgements

Notes and references

1 P. Roy, A. Ghosh, F. Barclay, A. Khare and E. Cuce, *Coatings*, 2022, **12**, 1089.
2 M. Wang, W. Wang, B. Ma, W. Shen, L. Liu, K. Cao, S. Chen and W. Huang, *Nano-Micro Lett.*, 2021, **13**, 62.
3 X. Lupa, X. Liu and L. Han, *Next Energy*, 2023, **1**, 100011.
4 F. D. Angelis, *Nat. Photonics*, 2021, **6**, 1586–1587.
5 M. A. Green, A. W. Y. Ho-Baillie and H. J. Snaith, *Nat. Photonics*, 2014, **8**, 506–514.
6 M. Roknuzzaman, J. A. Alarco, H. Wang, A. Du, T. Tesfamichael and K. K. Ostrikov, *Comput. Mater. Sci.*, 2019, **169**, 109118.
7 H. M. Ane, D. Y. Lee, J. Kim, G. Kim, K. S. Lee, J. Kim, M. J. Paik, Y. K. Kim, K. S. Kim, M. G. Kim, T. J. Shin and S. I. Seok, *Nature*, 2021, **598**, 444–450.
8 K. Yoshikawa, H. Kawasaki, W. Yoshida, T. Irie, K. Konishi, K. Nakano, T. Uto, D. Adachi, M. Kanematsu, H. Uzu and K. Yamamoti, *Nat. Energy*, 2017, **2**, 17032.
9 P. Tockhorn, J. Sutter, A. Cruz, P. Wagner, K. Jäger and D. Yoo, *Nat. Nanotechnol.*, 2022, **17**, 1214–1221.
10 M. Roknuzzaman, K. Ostrikov, H. Wang, A. Du and T. Tesfamichael, *Sci. Rep.*, 2017, 7, 14025.
11 W. Ke and M. G. Kanatzidis, *Nat. Commun.*, 2019, **10**, 965.
12 J. U. Rehman, M. Usman, S. Amjid, M. Sagir, M. B. Tahir, A. Hussain, I. Alam, R. Nazir, H. Alrobei, S. Ullah and M. A. Assiri, *Comput. Theor. Chem.*, 2022, **1209**, 113624.
13 O. Das, M. Saiduzzaman, K. M. Hossain, I. K. Shuvo, M. M. Rahman, S. Ahmad and S. K. Mitro, *Results Phys.*, 2023, **44**, 106212.
14 R. K. Pingak, *Comput. Condens. Matter*, 2022, **33**, e00747.
15 M. A. Rashid, M. Saiduzzaman, A. Biswas and K. M. Hossain, *Eur. Phys. J. Plus*, 2022, **137**, 649.
16 M. H. Rahman, M. Jubair, M. Z. Rahman, M. S. Ahasan, K. K. Ostrikov and M. Roknuzzaman, *RSC Adv.*, 2022, **12**, 7497–7505.
17 S. Khan, N. Mehmood, R. Ahmad, A. Kalsoom and K. Hameed, *Mater. Sci. Semicond. Process.*, 2022, **150**, 106973.

18 R. K. Pingak, A. Harbi, M. Moutaabbid, A. Z. Johannes, N. U. J. Hauwali, M. Bukit, F. Nitti and M. Z. Ndii, *Mater. Res. Express*, 2023, **10**, 095507.

19 A. E. Maughan, A. M. Ganose, M. M. Bordelon, E. M. Miller, D. O. Scanlon and J. R. Neilson, *J. Am. Chem. Soc.*, 2016, **138**, 8453–8464.

20 S. U. Zaman, S. Khan, N. Mehmood, A. U. Rahman, R. Ahmad, N. Sultan, F. Ullah and H. J. Kim, *Opt. Quantum Electron.*, 2022, **54**, 396.

21 F. Yousefzadeh, Q. A. Yousif, M. Ghanbari and M. Salavati-Niasari, *J. Mol. Liq.*, 2022, **349**, 118443.

22 D. J. Singh, *J. Appl. Phys.*, 2012, **112**, 083509.

23 G. Paolo, B. Stefano, B. Nicola, C. Matteo, C. Roberto, C. Carlo, C. Davide, C. Guido, C. Matteo, D. Ismaila, D. C. Andrea, d. G. Stefano, F. Stefano, F. Guido, G. Ralph, G. Uwe, G. Christos, K. Anton, L. Michele, M.-S. Layla, M. Nicola, M. Fransesco, M. Riccardo, P. Stefano, P. Alfredo, P. Lorenzo, S. Carlo, S. Sandro, S. Gabriele, P. S. Ari, S. Alexander, U. Paolo and M. Renata, *J. Phys.: Condens.Matter*, 2009, **21**, 395502.

24 W. Khon and L. J. Sham, *Phys. Rev.*, 1965, **140**, A1133.

25 J. P. Perdew, K. Burke and M. Ernzerhof, *Phys. Rev. Lett.*, 1996, **77**, 3865.

26 M. Råsander and M. A. Moram, *J. Chem. Phys.*, 2015, **143**, 144104.

27 F. Birch, *Phys. Rev.*, 1974, **71**, 809.

28 D. P. Hastuti, P. Nurwantoro and S. Sholihun, *Mater. Today Commun.*, 2019, **19**, 459–463.

29 G. K. Madsen and D. J. Singh, *Comput. Phys. Commun.*, 2006, **175**, 67–71.

30 M. A. Green, Y. Jiang, A. M. Soufianj and A. Ho-Baillie, *J. Phys. Chem. Lett.*, 2015, **6**, 4774–4785.

31 C. Ambrosch-Draxl and J. O. Sofo, *Comput. Phys. Commun.*, 2006, **175**, 1–14.

32 S. Bouhmaidi, A. Marjaoui, A. Talbi, M. Zanouni, K. Nouneh and L. Setti, *Comput. Condens. Matter*, 2022, **31**, e00663.

33 S. Bouhmaidi, R. K. Pingak, A. Azouaoui, A. Harbi, M. Moutaabbid and L. Setti, *Solid State Commun.*, 2023, **369**, 115206.

34 M. S. Alam, M. Saiduzzaman, A. Biswas, T. Ahmed, A. Sultan and K. M. Hossain, *Sci. Rep.*, 2022, **12**, 8663.

35 R. K. Pingak, S. Bouhmaidi, L. Setti, B. Pasangka, B. Bernandus, H. I. Sutaji, F. Nitti and M. Z. Ndii, *Indones. J. Chem.*, 2023, **23**, 843–862.

36 Q. Mahmood, F. hedhili, S. Al-Shomar, S. Chebaaneef, T. I. Al-Muhimeed, A. AlObaid, A. Meta and O. A. Alamri, *Phys. Scr.*, 2021, **96**, 095806.

37 R. K. Pingak, S. Bouhmaidi and L. Setti, *Phys. B*, 2023, **663**, 415003.

38 S. Bouhmaidi, A. Azouaoui, N. Benzakour, A. Hourmatallah and L. Setti, *Comput. Condens. Matter*, 2022, **33**, e00756.

39 M. Saiduzzaman, T. Ahmed, K. Hossain, A. Biswas, S. Mitro, A. Sultana, M. Alam and S. Ahmad, *Mater. Today Commun.*, 2023, **34**, 105188.

40 S. Bouhmaidi, M. B. Uddin, R. Pingak, S. Ahmad, M. Rubel, A. Hakamy and L. Setti, *Mater. Today Commun.*, 2023, **37**, 107025.

41 M. Ahmad, G. Rehman, L. Ali, M. Shafiq, R. Iqbal, R. Ahmad, T. Khan, S. Jalali-Asadabadi, M. Maqbool and I. Ahmad, *J. Alloys Compd.*, 2023, **705**, 828–839.

42 T. Ou, W. Jiang, Q. Zhuang, H. Yan, S. Feng, Y. Sun, P. Li and X. Ma, *Phys. B*, 2023, 415050.

43 A. Harbi and M. Moutaabbid, *Polyhedron*, 2023, **233**, 116316.

44 K. Chen, S. Schunemann, S. Song and H. Tuysuz, *Chem. Soc. Rev.*, 2018, **47**, 7045–7077.

45 A. Harbi, A. Aziz and M. Moutaabbid, *Inorg. Chem. Commun.*, 2023, **153**, 110842.

46 A. Hedhili, B. Hassan, M. S. Rashid, M. Bakr, Q. Mahmood, S. M. Al-Shomar, W. Alahmad, F. Alimi and L. Mechi, *Curr. Appl. Phys.*, 2023, **53**, 1–8.

47 A. Harbi, S. Bouhmaidi, R. K. Pingak, L. Setti and M. Moutaabbid, *Phys. B*, 2023, **668**, 415242.

48 C. Kaewmeechai, Y. Laosiritaworn and A. P. Jaroenjittichai, *Results Phys.*, 2022, **42**, 106015.

49 S. Bouhmaidi, A. Harbi, R. Pingak, A. Azouaoui, M. Moutaabbid and L. Setti, *Comput. Theor. Chem.*, 2023, **1227**, 114251.

50 T. Zelai, S. A. Rouf, Q. Mahmood, S. Bouzgarrou, M. A. Amin, A. I. Aljameel, T. Ghrib, H. H. Hegazy and A. Mera, *J. Mater. Res. Technol.*, 2022, **16**, 631–639.

51 A. Jehan, M. Husain, V. Tirth, A. Algahtani, M. Uzair, N. Rahman, A. Khana and S. M. Khan, *RSC Adv.*, 2023, **13**, 28395.

52 I. Pallikara, P. Kayastha, J. M. Skelton and L. D. Whalley, *Electron. Struct.*, 2022, **4**, 033002.

53 T. Wang, B. Daiber, J. M. Frost, S. A. Mann, E. C. Garnett, A. Walsh and B. Ehrler, *Energy Environ. Sci.*, 2017, **10**, 509–515.

54 X. Zhang, Y. Lv, Y. Lv, Y. Liu and Z. Yang, *J. Mater. Res. Technol.*, 2022, **17**, 425–432.

55 M. A. Hadi, M. N. Islam and J. Podder, *RSC Adv.*, 2022, **12**, 15461–15469.

56 A. Karmakar, G. M. Bernard, A. Meldrum, O. A. Oliynyk and V. K. Michaelis, *J. Am. Chem. Soc.*, 2020, **142**, 10780–10793.

57 X. Wu, X. Zhang, W. Yu, Y. Zhou, W. Wong, W. He, K. P. Loh, X.-F. Jiang and Q.-H. Xu, *J. Mater. Chem. A*, 2023, **11**, 4292–4301.

58 A. Harbi and M. Moutaabbid, *J. Supercond. Novel Magn.*, 2022, **35**, 3447–3456.

59 A. Harbi, A. Azouaoui, S. Benmokhtar and M. Moutaabbid, *J. Supercond. Novel Magn.*, 2022, **35**, 1405–1412.

60 A. Harbi, A. Azouaoui, Y. Toual, A. Hourmatallah and M. Moutaabbid, *J. Supercond. Novel Magn.*, 2023, **36**, 1171–1179.

61 H. Dong, C. Ran, W. Gao, M. Li, Y. Xia and W. Huang, *eLight*, 2023, **3**, 3.

62 S. Bouhmaidi, R. Pingak and L. Setti, *Moroccan J. Chem.*, 2023, **11**, 1254–1265.

63 M. Wuttig, C.-F. Schön, M. Schumacher, J. Robertson, P. Golub, E. Bousquet, C. Gatti and J.-Y. Raty, *Adv. Funct. Mater.*, 2022, **32**, 2110166.

64 M. Born, *Math. Proc. Cambridge Philos. Soc.*, 1940, **36**, 160–172.

65 R. R. Reddy, K. R. Gopal, K. Narasimhulu, L. S. S. Reddy, K. R. Kumar, G. Balakrishnaiah and M. R. Kumar, *J. Alloys Compd.*, 2009, **473**, 28–35.

66 K. Li, C. Kang and D. Xue, *Mater. Res. Bull.*, 2012, **47**, 2902–2905.

67 Z. Song, W. Fan, C. S. Tan, Q. Wang, D. Nam, D. H. Zhang and G. Sun, *New J. Phys.*, 2019, **21**, 073037.

68 H. M. Ghaithan, Z. A. Alahmed, S. H. M. Qaid and A. S. Aldwayyan, *ACS Omega*, 2021, **6**, 30752–30761.

69 S. F. Pugh, *London, Edinburgh Dublin Philos. Mag. J. Sci.*, 1954, **45**, 823–843.

70 Y. F. Cherif, M. Rouaighia, A. Zaoui and A. Boukortt, *Acta Phys. Pol., A*, 2017, **131**, 406–413.

71 M. A. H. Shah, M. Nuruzzaman, A. Hossain, M. Jubair and M. A. K. Zilani, *Comput. Condens. Matter*, 2023, **34**, e00774.

72 B. Ghebouli, M. A. Ghebouli, A. Bouhemadou, M. Fatmi, R. Khenata, D. Rached, T. Ouahrani and S. Bin-Omran, *Solid State Sci.*, 2012, **14**, 903–991.

73 M. E. A. Monir and F. Z. Dahou, *SN Appl. Sci.*, 2020, **2**, 465.

74 N. Erum and M. A. Iqbal, *Acta Phys. Pol., A*, 2020, **138**, 509–517.

75 A. Bakar, A. O. Alrashdi, M. M. Fadhali, A. Afaq, H. A. Yakout and M. Asif, *J. Mater. Res. Technol.*, 2022, **19**, 4233–4241.

76 A. A. Mubarak and S. Al-Omari, *J. Magn. Magn. Mater.*, 2015, **382**, 211–218.

77 M. Szafranski and A. Katrusiak, *J. Phys. Chem. Lett.*, 2016, **7**, 3458–3466.

78 S. Sun, F. H. Isikgor, Z. Deng, F. Wei, G. Kieslich, P. D. Bristowe, J. Ouyang and A. K. Cheetham, *ChemSusChem*, 2017, **10**, 3740–3745.

79 Z. Li, Y. Qin, L. Dong, K. Li, Y. Qiao and W. Li, *Phys. Chem. Chem. Phys.*, 2020, **22**, 12706–12712.

80 A. Biswas, M. S. Alam, A. Sultana, T. Ahmed, M. Saiduzzaman and K. M. Hossain, *Appl. Phys. A: Mater. Sci. Process.*, 2021, **127**, 939.

81 M. Z. Rahaman and A. Hossain, *RSC Adv.*, 2018, **8**, 33010–33018.

82 D. R. Penn, *Phys. Rev.*, 1962, **128**, 2093–2097.

83 H. M. Ghaithan, Z. A. Alahmed, S. M. H. Qaid, M. Hezam and A. S. Aldwayyan, *ACS Omega*, 2020, **5**, 7468–7480.

84 Y. M. Odeh, S. M. Azar, A. Y. Al-Reyahi, A. A. Mousa, E. K. Jaradat and N. Al Aqtash, *AIP Adv.*, 2023, **13**, 075118.

85 T. Oku, M. Zushi, Y. Imanishi, A. Suzuki and K. Suzuki, *Appl. Phys. Express*, 2014, **7**, 121601.

86 S. Piskunov, A. Gopeyenko, E. Kotomin, Y. Zhukovskii and D. Ellis, *Comput. Mater. Sci.*, 2007, **41**, 195–201.

87 A. Z. Johannes, R. K. Pingak and M. Bukit, *IOP Conf. Ser.: Mater. Sci. Eng.*, 2020, **823**, 012030.

88 Y. Selmani, H. Labrim, A. Jabar and L. Bahmad, *Int. J. Mod. Phys. B*, 2023, 2450334.